Chaos in the 'Sliced Cone' Model of Wind-driven Ocean Circulation

Andrew Kiss

1   Introduction

Recent analytical and numerical results by Salmon [Salmon, 1992] and Becker and Salmon [Becker and Salmon, 1997] have shown that the barotropic flow in simple β-plane models of wind-driven ocean circulation is dramatically altered when the vertical boundaries usually employed in such models are replaced by continental slopes on which the depth goes gradually to zero at the boundaries. The sloping topography acts to guide the barotropic flow and moves the western boundary currents away from the lateral boundaries and onto the lower part of the slope. This produces a vorticity distribution which is more prone to instabilities than in the case of vertical sidewalls and diminishes the role of lateral viscosity at the boundary in dissipating potential vorticity, leaving Ekman friction as the dominant dissipation mechanism.

   The 'sliced cone' model was introduced by Griffiths and Veronis [Griffiths and Veronis, 1997] to investigate the effect of sloping sidewalls on homogeneous wind-driven flow on a simulated β-plane in the laboratory. This model is a variant of Pedlosky and Greenspan's 'sliced cylinder' model [Pedlosky and Greenspan, 1967] in which the vertical sidewalls have been replaced by an azimuthally uniform slope around the perimeter of the basin. The presence of closed geostrophic contours provides a "short cut" for the western boundary current of the interior Sverdrup flow, allowing the current to delay dissipation of the potential vorticity imparted by the wind until just before it rejoins the interior flow.

   The laboratory results showed that the flow can become unsteady when the wind stress forcing is anticyclonic and exceeds a critical strength. The fluctuations are periodic for moderately supercritical forcing, but become aperiodic under relatively strong forcing. This paper presents an analysis of the time dependence displayed by numerical simulations of the flow in this apparatus as a function of forcing strength.

2   The 'sliced cone' model

The laboratory model employed by Griffiths and Veronis [Griffiths and Veronis, 1997] utilized a basin of the form shown in Figure 1, filled with water and bounded above by a rigid horizontal lid. The base of the apparatus rotates with a constant angular velocity $\Omega \hat{\mathbf{k}}$ about a vertical axis, whilst the rigid lid has a slightly different angular velocity $(1 + \epsilon)\,\Omega \hat{\mathbf{k}}$ in order to simulate a spatially uniform wind stress curl. The sidewall has a 45° slope relative to the horizontal

and this cone is intersected by a plane with slope 1:10 which forms the central part of the bottom boundary. Figure 1 shows that in this geometry the geostrophic contours (contours of constant depth) are circles near the rim and D-shaped curves when they cross the interior. All geostrophic contours are closed curves, in contrast to the 'sliced cylinder' in which all geostrophic contours are blocked by the vertical sidewalls. The potential vorticity gradient imposed by the shallow slope in the interior is analogous to the potential vorticity gradient of a β-plane and allows us to identify directions in the apparatus with various points of the compass, as shown in the figure (note that the apparatus rotates in the northern hemisphere sense). The width $2a$ of the apparatus is 97.3 cm and the depth H at the center is 12.5 cm.
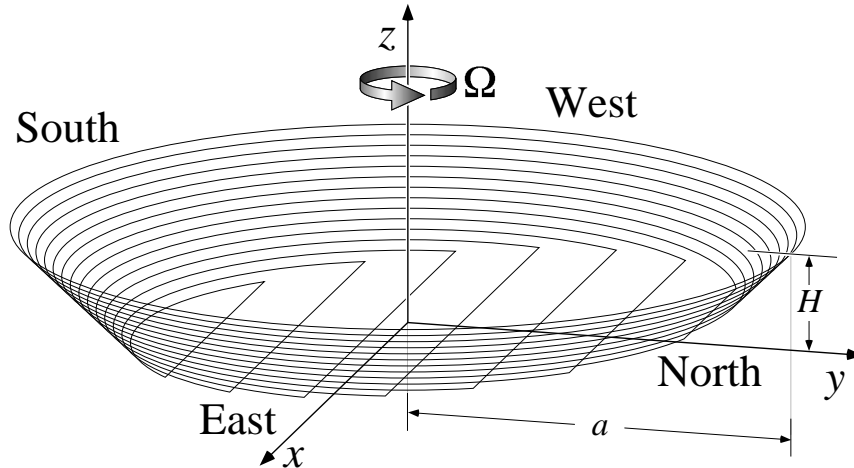

Figure 1: Perspective diagram of the 'sliced cone' model used in the laboratory and numerical experiments. The curves are contours of constant depth (geostrophic contours), and the compass directions are defined in terms of the potential vorticity gradient imposed by the sloping bottom in the interior.

The type of flow seen in this apparatus depends on ϵ and the Ekman number $E = \frac{\nu}{\Omega H^2}$, where ν is the kinematic viscosity of the fluid (water in our case). We can also define a Rossby number by $Ro = |\epsilon|$. A linear analysis (Ro=0) based on an expansion in powers of $E^{\frac{1}{2}}$ was presented in [Griffiths and Veronis, 1998]. This analysis showed that the zeroth order flow is along geostrophic contours, and is therefore about ten times faster on the slope than in the interior due to the order of magnitude difference of the bottom slopes in these regions. The $E^{\frac{1}{2}}$-order correction introduces the effect of wind forcing in the interior, resulting in a cross-contour Sverdrup flow which gives a northwest-southeast tilt to the streamlines in the interior but relatively little change to the slope current. At the next order a Stewartson $E^{\frac{1}{4}}$ layer at the junction between the rapid slope current and the slow interior flow makes the azimuthal velocity continuous in this region.

The laboratory study by Griffiths and Veronis [Griffiths and Veronis, 1997] showed that the sign of ϵ has a dramatic effect on the stability of the flow at finite Ro, through a mechanism clarified by the numerical investigation of [Kiss and Griffiths, 1998]. When $\epsilon > 0$ (cyclonic

forcing) the circulation was steady for all values of Ro and E investigated. Under anticyclonic forcing ($\epsilon < 0$) the slope current enters the interior as a jet when Ro is large, and the flow becomes unstable for large enough Ro and small enough E. The laboratory results showed that there are four main regimes as a function of Ro and E for anticyclonic forcing. For small Ro the asymptotic state after spin-up is a steady circulation (apart from some extremely small-amplitude fluctuations seen in the laboratory which the numerical model used here did not reproduce). The flow becomes unstable at a critical value of Ro, which depends on the value of E. For large Ro the only instability which appears is a pinching-off of cyclonic eddies from the cyclonic meander in the western boundary current jet. At small E the situation is more complicated: the first instability to appear is a growing wave in the anticyclonic shear layer at the the west of the interior, in which anticyclonic eddies appear at the west and grow as they are advected northwards until they dissipate when they collide with the southern edge of the jet. At larger values of Ro the cyclonic loop in the jet also becomes unstable and sheds cyclonic eddies. Initially both the cyclonic and anticyclonic instabilities are periodic, but at large Ro the flow for any E appears to become chaotic.

These laboratory observations raise interesting questions as to the nature of the transitions between these regimes, and the route to chaos in this system. This research project was a numerical investigation of these transitions, using the techniques of dynamical systems theory in an approach similar to that of [Jiang et al., 1995, Meacham and Berloff, 1997, Berloff and Meacham, 1997]. The behavior of the system under anticyclonic forcing was studied as a function of Ro at a fixed value of E (1.5075×10^{-5}). This value was chosen in order to study the more interesting situation in which both cyclonic and anticyclonic eddy shedding can appear. In the next two sections the formulation and implementation used in the numerical model are discussed; the rest of this paper is devoted to a presentation and discussion of the methods used and the results obtained.

2.1   Formulation

The equations of motion for this system (relative to coordinates rotating with angular velocity $\Omega\hat{\mathbf{k}}$) are:

$$\partial \mathbf{u} t + Ro \left(\mathbf{u} \cdot \nabla\right) \mathbf{u} + 2\hat{\mathbf{k}} \times \mathbf{u} = -\nabla p + E\nabla^2 \mathbf{u} \tag{1}$$

and

$$\nabla \cdot \mathbf{u} = 0, \tag{2}$$

where $\hat{\mathbf{k}}$ is the unit vector in the z direction (vertical), p is the pressure divided by the density and we have scaled the velocity $\mathbf{u}$, time t and length by $U = |\epsilon\Omega H|$, $|\Omega^{-1}|$ and H, respectively. The importance of advection and viscosity are parameterized by the Rossby number $Ro = \frac{U}{\Omega H} = |\epsilon|$ and Ekman number $E = \frac{\nu}{\Omega H^2}$, respectively, where ν is the kinematic viscosity of the fluid. Gravitational and centrifugal accelerations are not relevant to this system, since there is no free surface and no stratification.

We shall separate the vertical and horizontal components of the velocity by writing $\mathbf{u} = \mathbf{u}_H + \hat{\mathbf{k}}w$, where $\hat{\mathbf{k}} \cdot \mathbf{u}_H = 0$. For the parameters used in this study it is a very good approximation to assume (outside the Ekman layers) that $\mathbf{u}_H$ is independent of z and horizontally

nondivergent, so we have

$$\mathbf{u}_H = \hat{\mathbf{k}} \times \nabla_H \psi, \tag{3}$$

where ψ is the streamfunction and ∇_H denotes the horizontal gradient operator.

Taking the vertical component of the curl of the momentum equation 1 yields an equation for the vertical vorticity ζ:

$$\partial \zeta t + Ro\, J(\psi, \zeta) = (2 + Ro\, \zeta)\, \partial wz + E\nabla_H^2 \zeta, \tag{4}$$

where

$$\zeta = \nabla_H^2 \psi \tag{5}$$

and $J(a, b) \equiv \partial ax \partial by - \partial ay \partial bx$ is the two-dimensional Jacobian operator. The assumption that $\partial \mathbf{u}_H z = \mathbf{0}$ implies (via 2) that $\frac{\partial^2 w}{\partial z^2} = 0$, allowing us to find ∂wz by using steady, linear Ekman matching conditions[1] for w at the top and bottom boundaries. Since the bottom slope is not small, a coordinate-free form of equation (4.9.32) in [Pedlosky, 1987] (valid where the radius of curvature of the bottom topography is much larger than the Ekman layer thickness) was used to find w on the bottom boundary. Combining this with the upper Ekman matching condition yields

$$\partial wz = \frac{E^{\frac{1}{2}}}{2(1-h)}\left(\zeta_T - (1+\sigma)\zeta - s\sigma J\big(s^{-1}J(\psi,h),h\big)\right) - \frac{J(\psi,h)}{(1-h)}, \tag{6}$$

where $\zeta_T = 2\frac{\epsilon}{|\epsilon|}$ is the vorticity of the lid, $1 - h$ is the scaled fluid depth, $s = |\nabla_H h|$ is the bottom slope and $\sigma = \left(1 + s^2\right)^{\frac{1}{4}}$. On the sloping sidewall we have $\partial h\theta = 0$ (where θ is the azimuthal coordinate) and 6 has the form

$$\partial wz = \frac{E^{\frac{1}{2}}}{2(1-h)}\left(\zeta_T - (1+\sigma)\zeta - \frac{s^2\sigma}{r^2}\frac{\partial^2 \psi}{\partial\theta^2}\right) - \frac{J(\psi,h)}{(1-h)}, \tag{7}$$

where r is the radial coordinate. In the interior the bottom slope is so small that its effect on the bottom Ekman layer can be neglected, giving

$$\partial wz = \frac{E^{\frac{1}{2}}}{2(1-h)}\left(\zeta_T - 2\zeta\right) - \frac{J(\psi,h)}{(1-h)}. \tag{8}$$

The no-slip boundary condition gives

$$\psi = \partial \psi r = 0 \qquad \text{at}\ \ r = \frac{a}{H}. \tag{9}$$

---

[1]Steady, linear Ekman matching is valid for flows which are nearly steady over one rotation period [Beardsley, 1975b] and have $Ro \ll E^{\frac{1}{4}}$ [Bennetts and Hocking, 1973]. The latter criterion is violated for the more strongly forced results presented here, but the close similarity of the calculated flows to those seen in the laboratory suggests that the error involved in using linear Ekman conditions is insignificant. Thus it was felt that using the much more complicated nonlinear Ekman conditions was not justified for our purposes.

2.2 The numerical model

The numerical experiments were conducted with a highly efficient sliced-cylinder code developed by Page [Page, 1982] and described in detail in his PhD thesis [Page, 1981]. The algorithm is the same as that presented by Beardsley [Beardsley, 1975a], which was in turn based on the refinement by Israeli [Israeli, 1970] of a scheme proposed by Pearson [Pearson, 1965]. For this study the code was modified to include the effect of the sloping sidewalls on the bottom Ekman layer. The code solves 4 and 5, where ∂wz is found by using 7 on the slope[2] and 8 in the interior. This system generalizes that analyzed in [Griffiths and Veronis, 1998] by including advection, lateral viscosity and time dependence. Spatial derivatives are calculated using second-order centered differences on a polar grid, except at the origin where an integral treatment is used. The vorticity equation 4 is solved using the alternating-direction implicit method, and a fast Fourier transform in θ is used to solve the Poisson equation 5 for ψ. Since the nonlinearity in 4 couples it to 5, these equations are solved iteratively within each timestep until both ψ and ζ converge. This in-timestep iteration also serves to converge ζ at the boundary to a value which is consistent with the no-slip boundary condition 9, using optimal relaxation. The algorithm is unconditionally stable for zero Ro and retains its stability for all reasonable values of Ro. The numerical results reported here were obtained using 160 grid points in the radial direction and 512 in the azimuthal direction (with no stretching in either direction) and a timestep of $10^{-3}E^{-\frac{1}{2}} \approx \frac{1}{8}$ rotation periods, giving good spatial and temporal resolution. A comparison of numerical and laboratory results for the northward velocity under cyclonic forcing is shown in Figure 2.

3 Methods

Although some use was made of sequences of snapshots of the ψ and ζ fields, the primary diagnostic we used to study the time dependence of the computed flows was the basin integral of the kinetic energy, $K(t) = -\iint \psi(t)\zeta(t)dA$. Another quantity plotted in the following section is the normalized fluctuation in K, $K'(t) = \frac{K(t)-\bar{K}}{\bar{K}}$, where $\bar{K}$ is the time-average of K in the statistically steady state. Time series of K' calculated at each time step were analyzed by several techniques:

3.1 Power spectra

Power spectra of the time series allowed identification of the primary frequencies present, and provided a means of discriminating between quasiperiodic and chaotic time series.

3.2 Delay coordinates

The spatial resolution used in the model implies that this numerical system has a phase space with over 80000 dimensions. However as we shall see the trajectory of the state vector is confined to a manifold with a much smaller dimension than that of the full phase

---

[2] 7 is not evaluated on the lateral boundary itself (where $1 - h$ vanishes) because this is where 9 is imposed
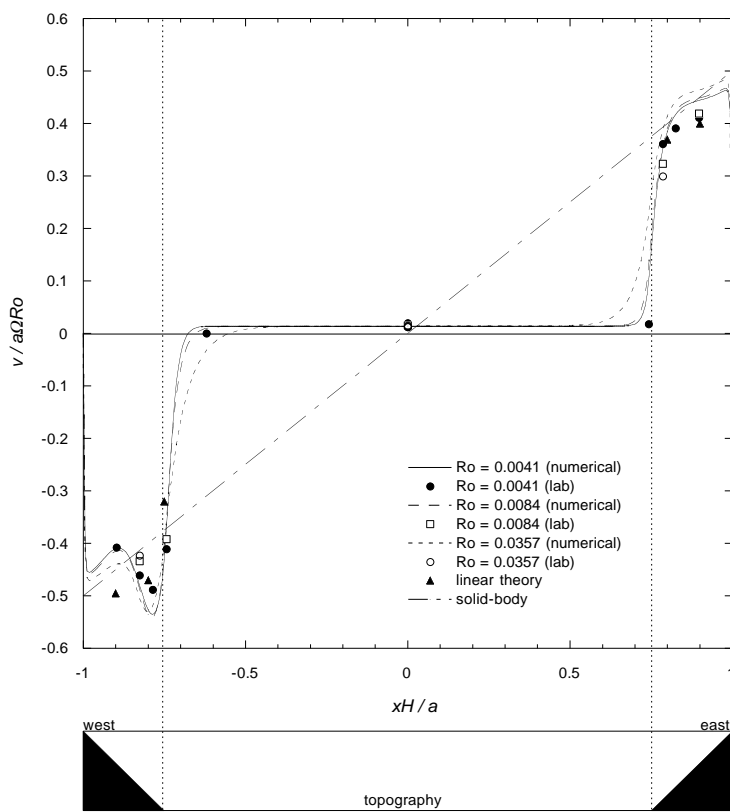
Figure 2: Laboratory and theoretical results from [Griffiths and Veronis, 1997] and [Griffiths and Veronis, 1998] compared with numerical results for the northward component of the normalized velocity as a function of position along the line $y = 0$, for cyclonic forcing.

space. The technique of delay-space reconstruction allows a trajectory to be extracted from the time series which has the same topological properties as the trajectory in the full phase space [Takens, 1981]. The delay-space trajectory is constructed by forming the time-dependent n - dimensional vector $\mathbf{X}(t; \tau)$, whose components are $X_i = K'(t - (i-1)\tau)$, where τ is a fixed delay time. The topological properties of the trajectory are independent of the choice of τ, but in order to obtain a trajectory which is not too contorted it is best to choose τ so that X_i and X_{i+1} are neither strongly correlated nor strongly uncorrelated. The delay used in the results presented here was 7.52 days, about a quarter of the shortest period (25 to 31 days). Trajectories were produced using embedding dimensions n of 2 or 3.

3.3   Poincaré sections

We found Poincaré sections to be a useful diagnostic tool for studying the structure of phase space trajectories and the manner in which the system converged to its final state. They were constructed by choosing a plane of interest in delay space (say, $X_k = c$ for some component k) and recording the position at which the trajectory passed through the plane in the direction of increasing X_k. The set of these intersection points comprises a Poincaré section of the trajectory. The results presented here used $c = 0$, the asymptotic mean value of K'.

4   Results

Numerical results were obtained for many different Rossby numbers, concentrated about values of Ro corresponding to transitions between regimes. The numerical model was integrated until the system reached a statistically steady state (at least several hundred days, and longer when close to a bifurcation) and the integration was continued to obtain a long time series in order to study the time dependence of the asymptotic state. The results are summarized in Figure 3, which shows the time average $\bar{K}$ of the asymptotic basin-integrated kinetic energy as a function of Ro. It is clear that there are several transitions between regimes, which take place abruptly at critical values of the Rossby number. The most interesting region, in which the behavior changes from periodic to quasiperiodic and ultimately to chaotic, takes place over a relatively small range of Ro. Over some of this range there is a second branch of solutions. The details of these regimes and the transitions between them are discussed below.

4.1   Fixed point (steady flow)

For $Ro < Ro_1 \approx 8.5 \times 10^{-3}$ the flow converges to a steady state of the form shown in Figure 4, in which flow is closely aligned with depth contours on most of the slope and is driven across depth contours by the wind stress in the interior. These regions are joined by a region of strong anticyclonic vorticity at the bottom of the slope where dissipation of vorticity by the bottom Ekman layer allows flow across depth contours. The inertial overshoot where the slope current rejoins the interior at the west becomes more pronounced as Ro is increased. A time series of the normalized energy perturbation K' at $Ro = 1.0 \times 10^{-3}$ is shown in Figure 5. At this Rossby number the flow converges directly to the steady state without oscillations. Closer to the transition to unsteady flow the convergence is oscillatory (see Figure 6). The power spectrum of the extremely small-amplitude decaying oscillation at $Ro = 7.5 \times 10^{-3}$ shows that the oscillation frequency is around 0.027 cycles per day. This spectral peak has been labeled A for future reference.

4.2   Limit cycle (periodic flow)

When $Ro_1 < Ro < Ro_2 \approx 2.64 \times 10^{-2}$, the flow is unsteady and displays a periodic train of growing anticyclonic waves in the anticyclonic shear layer at the west. Close to the bifurcation point the oscillations in K' have an extremely small amplitude, as shown in Figure 7 for $Ro = 10^{-2}$. The frequency at $Ro = 10^{-2}$ is 0.032 cycles per day, close to that of the decaying
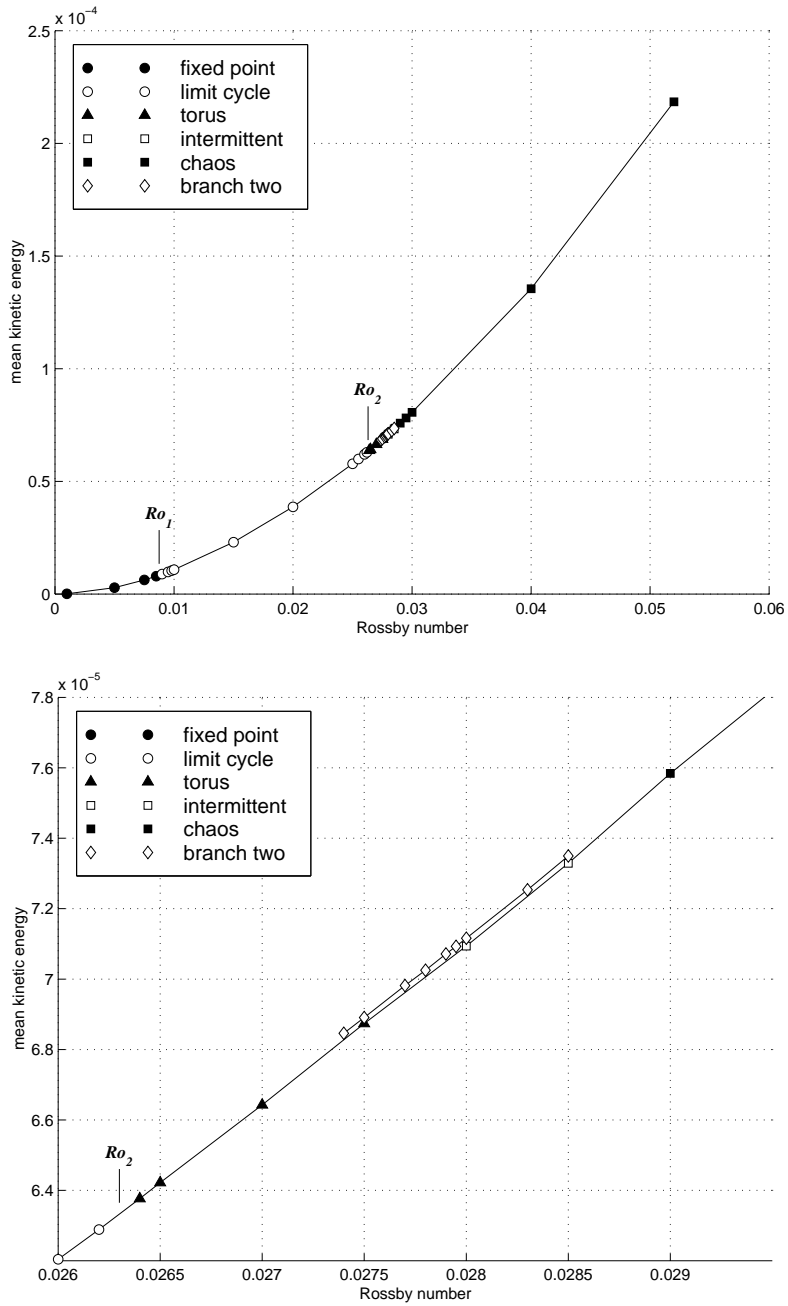
Figure 3: Time average $\bar{K}$ of the basin-integrated kinetic energy as a function of Ro. a) the complete range of Ro investigated; b) a closeup of the transition from a limit cycle to chaos, showing the presence of two branches for a range of Ro.
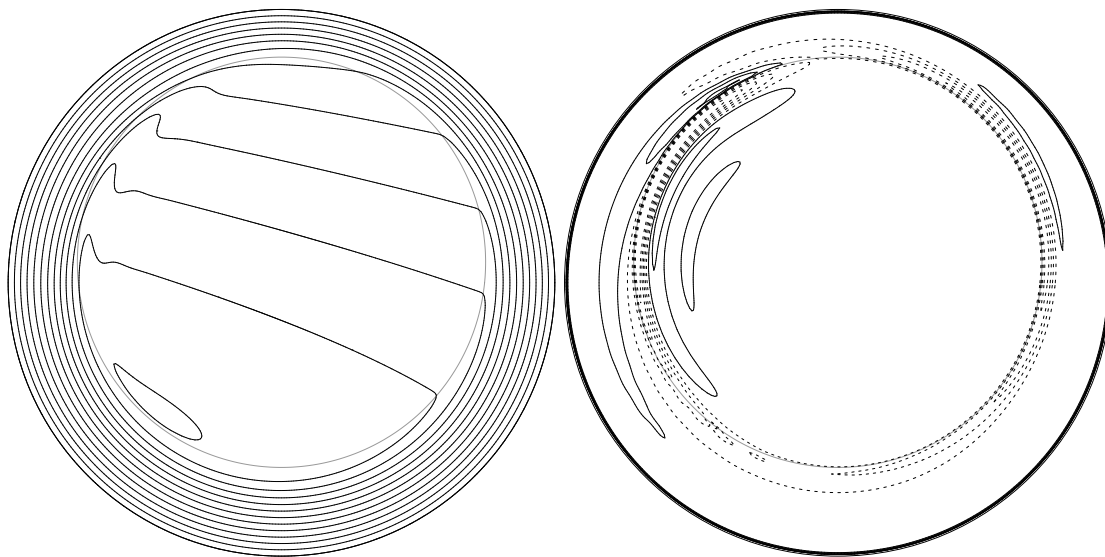
Figure 4: Contours of ψ (left) and ζ (right) for $Ro = 5 \times 10^{-3}$. Contours of anticyclonic ζ are dashed and the grey ellipse marks the bottom of the slope. North is at the top and the mean flow is clockwise.
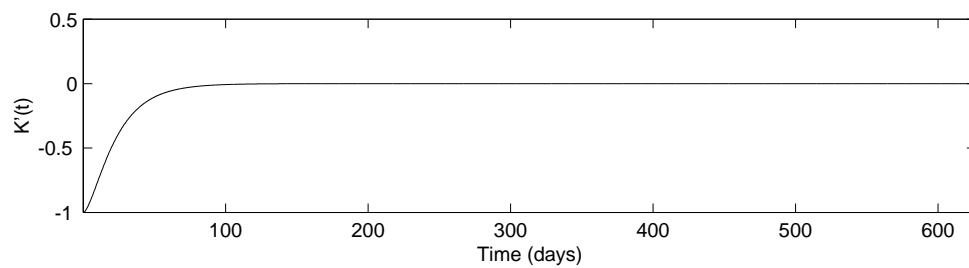

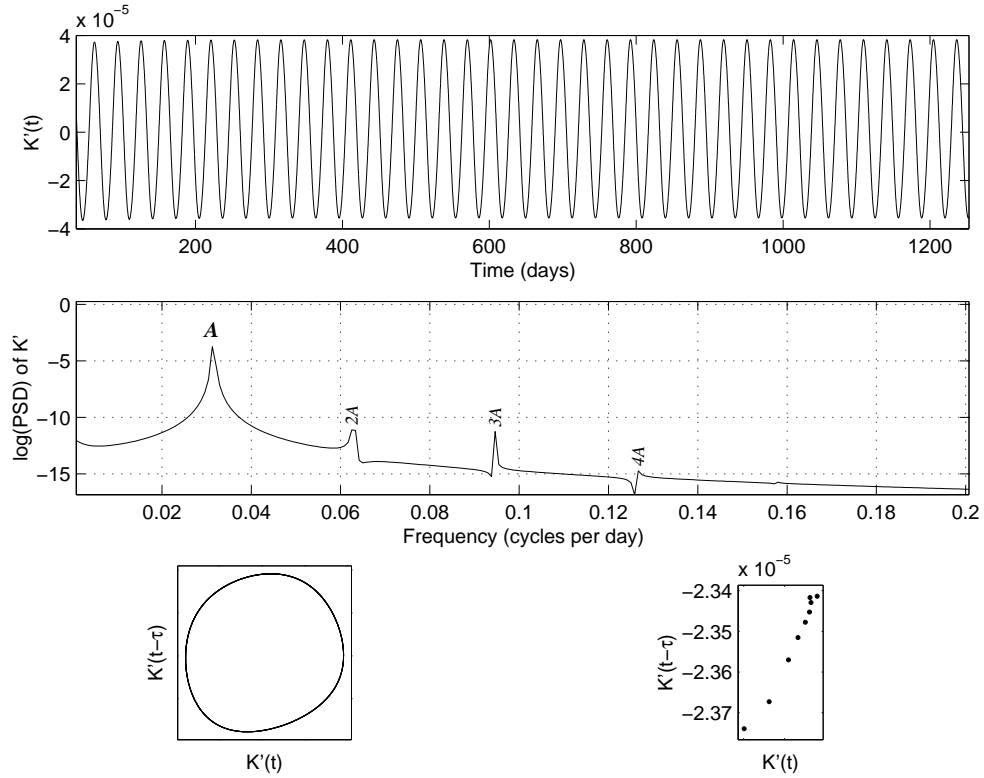Figure 5: Time dependence of K' with $Ro = 1.0 \times 10^{-3}$.
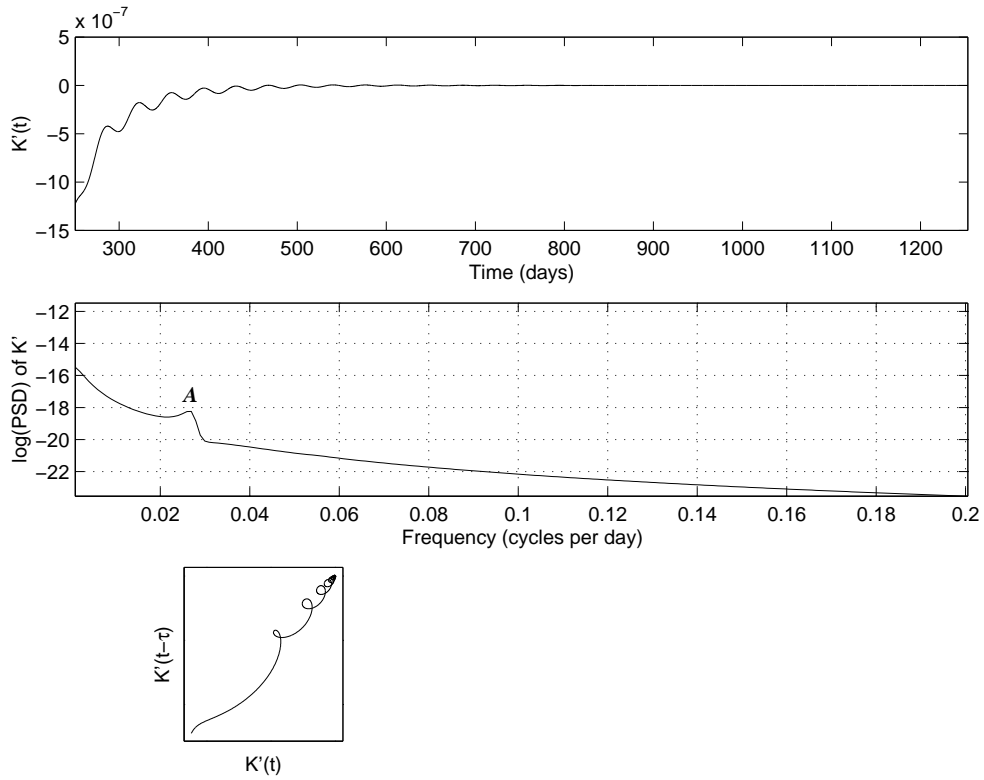
Figure 6: Time dependence of K' with $Ro = 7.5 \times 10^{-3}$. Top: time series; middle: power spectrum of time series (the zero frequency peak has been suppressed); bottom left: delay-space trajectory for the time series.

Figure 7: Time dependence of K' with $Ro = 1.0 \times 10^{-2}$. Top: time series; middle: power spectrum of time series (the zero frequency peak has been suppressed); bottom left: delay-space trajectory for the time series; bottom right: Poincaré section of the delay-space trajectory.

oscillation at $Ro = 7.5 \times 10^{-3}$. The other peaks in the power spectrum are harmonics of this fundamental frequency, as they must be for a periodic oscillation. The phase - space trajectory in Figure 7 has the form of a limit cycle; the Poincaré section (which has axes scaled to fit the range of the intersection points) shows that convergence to this invariant set does not involve any oscillations. These observations of time series for Ro in the vicinity of Ro_1 provide strong evidence that the onset of time-dependence takes place by a supercritical Hopf bifurcation at $Ro = Ro_1$.

The physical nature of the instability which occurs at Ro_1 can be seen by computing the average streamfunction field over one period and subtracting this from the instantaneous field at a given time. Mean and perturbation streamfunctions at $Ro = 9.5 \times 10^{-3}$ are shown in Figure 8. The perturbation streamlines are inclined into the mean velocity gradient in a manner consistent with extraction of energy from the mean flow, as discussed by Pedlosky [Pedlosky, 1987]. This barotropic instability is associated with the cross-flow extremum of the potential vorticity $q = (2 + Ro\zeta)/(1 - h)$ at the bottom of the slope, as discussed in [Kiss and Griffiths, 1998]. The positive perturbations in ψ coincide with regions of increased anticyclonic vorticity, and
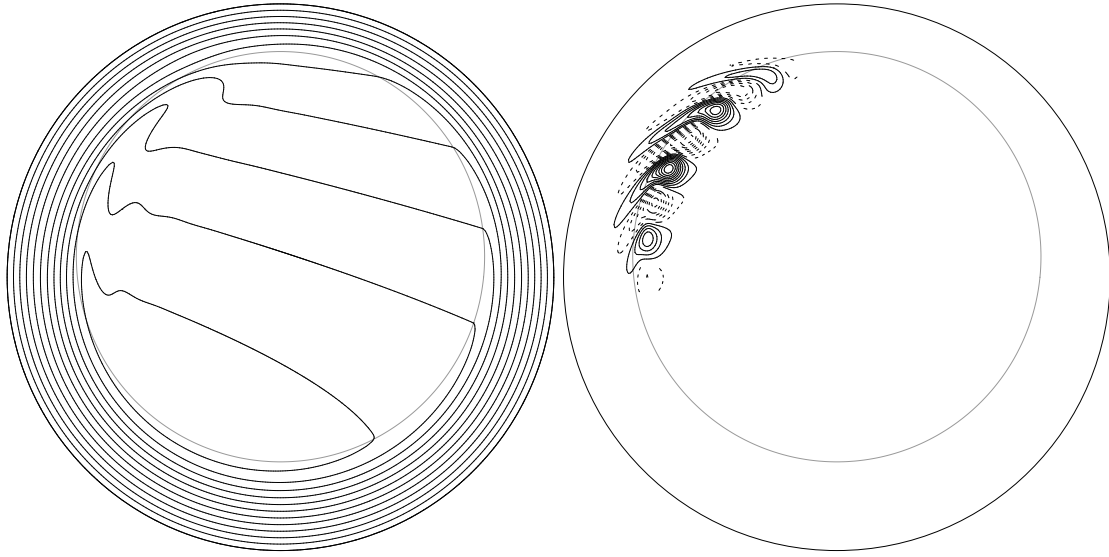
Figure 8: Contours of ψ averaged over one oscillation (left) and the difference in ψ from this field at one time (right; the contour interval has been reduced by a factor of 30). $Ro = 9.5 \times 10^{-3}$; contours of negative ψ are dashed and the grey ellipse marks the bottom of the slope. North is at the top and the mean flow is clockwise.

hence to maxima in the vorticity waves seen in the anticyclonic shear layer. The waves grow as they are advected northwards with the flow until they reach the end of the outflow region from the slope current, where they die out. Each kinetic energy peak corresponds to an anticyclone reaching its maximum amplitude before being advected into the region where it decays.

As Ro is increased towards Ro_2 the amplitude of the anticyclonic perturbations becomes larger, until they are sufficiently strong to produce closed contours of ψ, resulting in a northward-traveling train of anticyclonic eddies. The vorticity of the anticyclones acts to stretch out the jet when they arrive at its southern edge, making it extend southeastwards into the interior and intensifying its cyclonic meander. The jet then retracts back to its former length as each anticyclone dissipates, before being stretched again by the arrival of the subsequent anticyclone. When Ro is large enough, these periodic perturbations to the jet result in a cyclonic eddy pinching off from the cyclonic loop in the jet as each anticyclone dissipates. This process is shown in Figure 9, which shows snapshots of ζ at a local maximum and the following local minimum of K.

Figure 10 shows the time behavior at $Ro = 2.62 \times 10^{-2}$, just before the second bifurcation. The frequency has increased to 0.039 cycles per day, and the oscillation has a much larger amplitude but is still periodic. However in contrast to the case of $Ro = 10^{-2}$, the convergence to the limit cycle is now oscillatory, the decaying oscillation having a frequency of about 0.017 cycles per day. This new spectral peak will be denoted B.
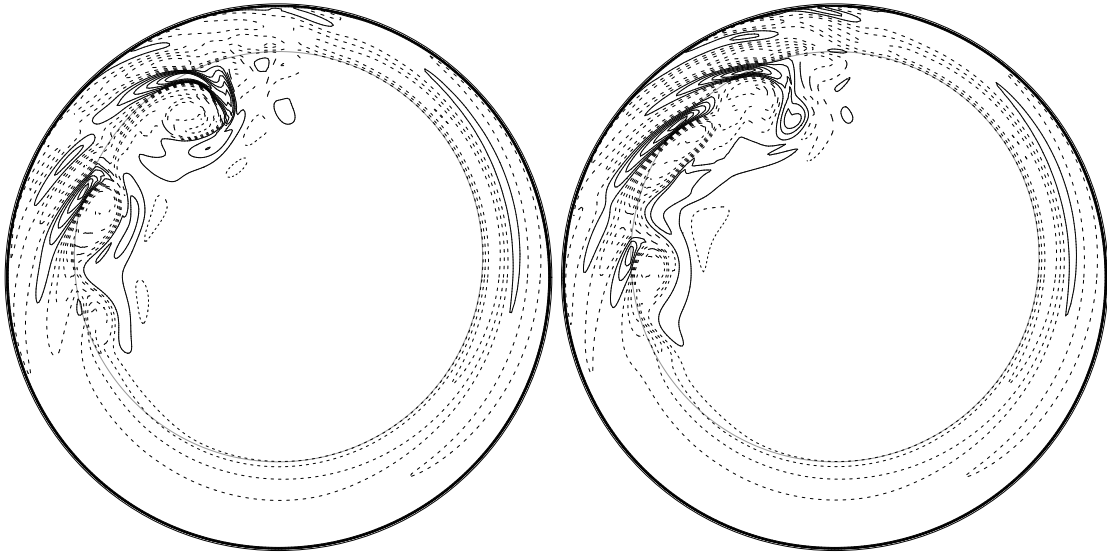
Figure 9: Contours of ζ at two different times for $Ro = 2.5 \times 10^{-2}$. Left: at a local maximum of K; right: at the subsequent minimum of K. Contours of negative ζ are dashed. Note how the strong anticyclone wraps a tongue of cyclonic vorticity around itself, which sheds a cyclonic eddy when the anticyclone dissipates. An animation of this sequence can be viewed at http://rses.anu.edu.au/gfd/link/AK/WHOIGFD.html

4.3   Torus (quasiperiodic or phase-locked flow)

A very slight increase in Ro from $Ro = 2.62 \times 10^{-2}$ to $Ro = 2.64 \times 10^{-2}$ produces a transition from periodic to quasiperiodic flow, giving a trajectory which is a torus, as shown in Figure 11. The oscillation denoted B is now no longer decaying, and appears as a peak in the power spectrum at a frequency which is indistinguishable from that of the decaying oscillation at $Ro = 2.62 \times 10^{-2}$. The winding number of the trajectory on the torus is $B/A = 0.433$. The numerous other peaks in the spectrum are cross-harmonics of A and B, as indicated in the figure. Once again, this transition seems to have taken place by a Hopf bifurcation. As for strongly forced periodic flow, relative maxima and minima of K' correspond respectively to the arrival of a large anticyclone at the southern side of the jet, and the subsequent shedding of a cyclone. This basic cycle has a period $1/A$, but is amplitude-modulated by the second period $1/B$, giving rise to the cross-harmonics of A and B in the power spectrum.

As Ro increases, the Poincaré section becomes an increasingly distorted loop, and the amplitude of the peak with frequency $A - 2B$ becomes larger. At $Ro = 2.70 \times 10^{-2}$ these long-period fluctuations are periodic, but at $Ro = 2.75 \times 10^{-2}$ the fluctuations appear to become aperiodic (although a longer time series would be needed to confirm this). Figure 12 shows the time dependence of the kinetic energy at $Ro = 2.75 \times 10^{-2}$, in which the peak at $A - 2B$ has become large, corresponding to the conspicuous variations with a period of about 500 days visible in the time series.
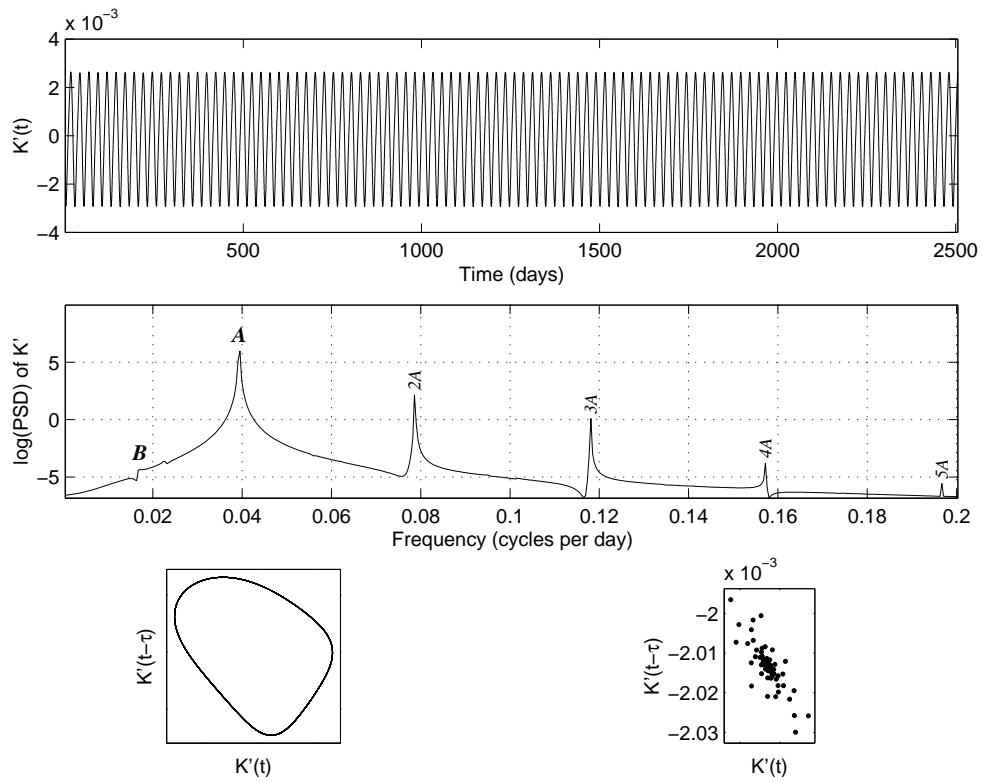
Figure 10: Time dependence of K' with $Ro = 2.62 \times 10^{-2}$. Top: time series; middle: power spectrum of time series (the zero frequency peak has been suppressed); bottom left: delay-space trajectory for the time series; bottom right: Poincaré section of the delay-space trajectory.
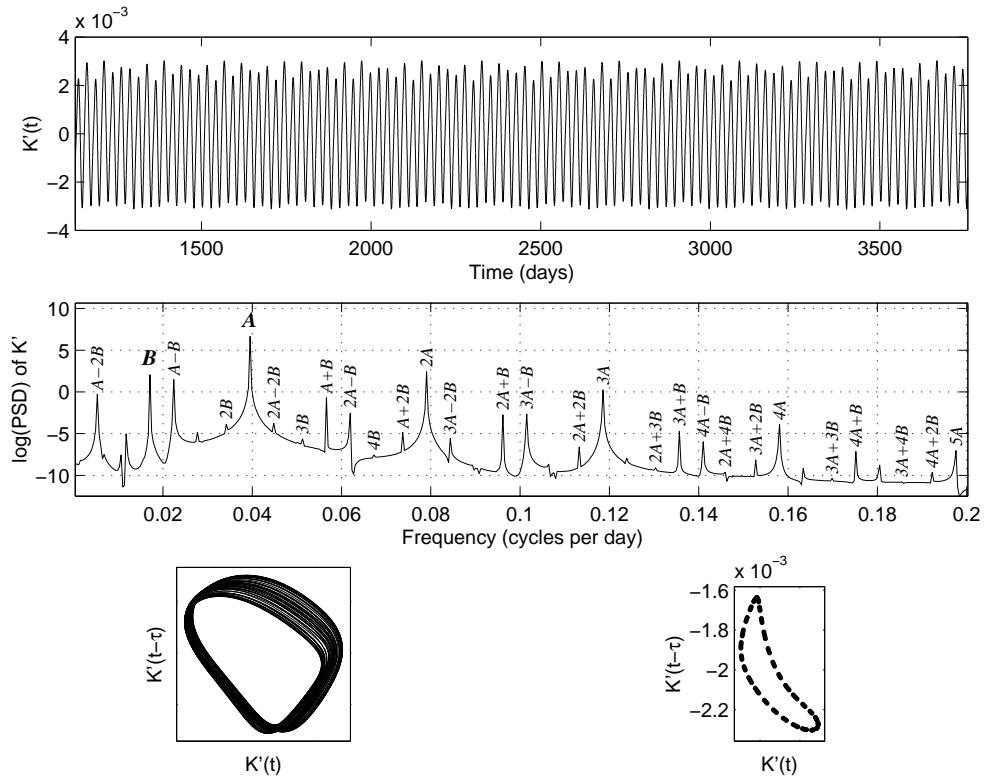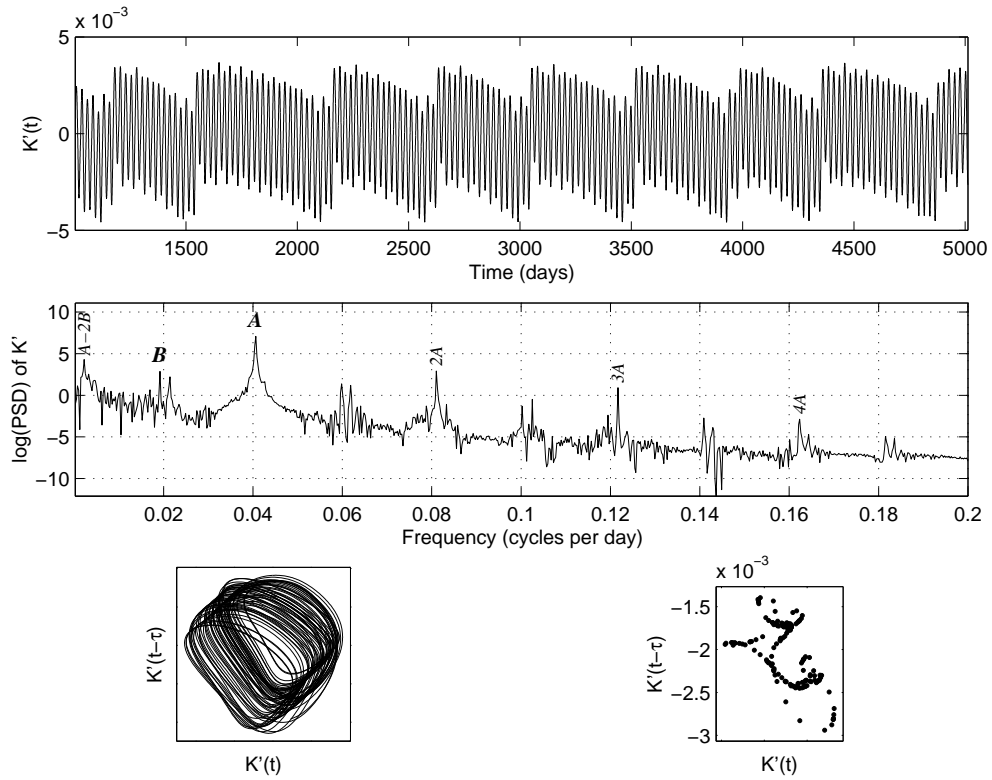
Figure 11: Time dependence of K' with $Ro = 2.64 \times 10^{-2}$. Top: time series; middle: power spectrum of time series (the zero frequency peak has been suppressed); bottom left: delay-space trajectory for the time series; bottom right: Poincaré section of the delay-space trajectory.

Figure 12: Time dependence of K' with $Ro = 2.75 \times 10^{-2}$. Top: time series; middle: power spectrum of time series (the zero frequency peak has been suppressed); bottom left: delay-space trajectory for the time series; bottom right: Poincaré section of the delay-space trajectory.
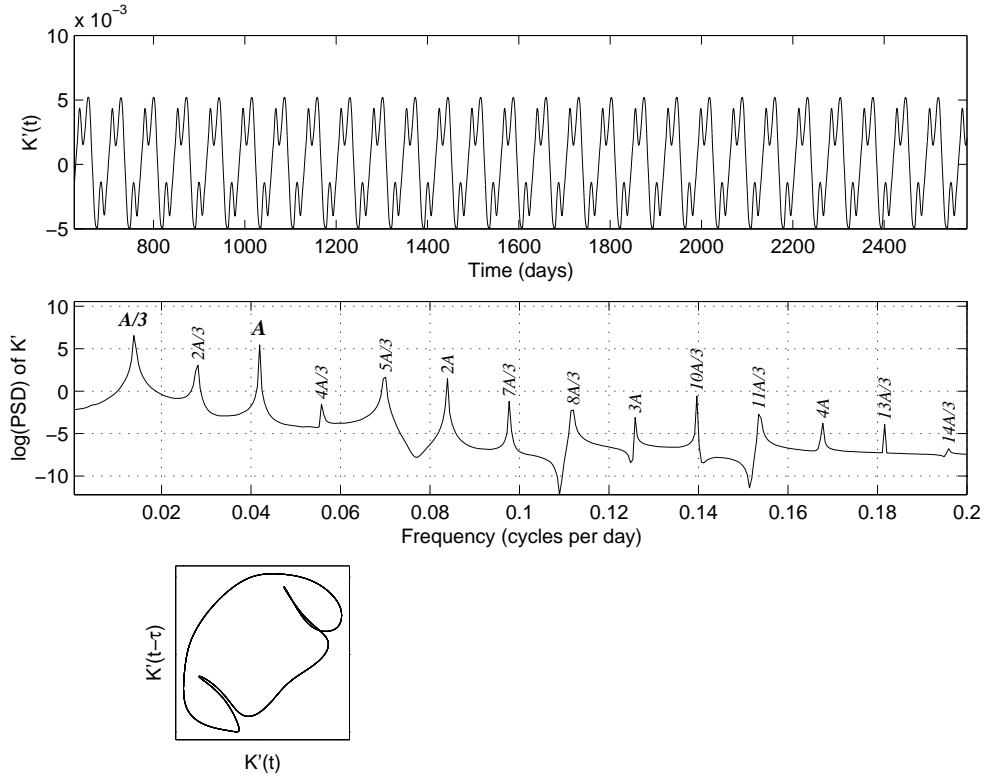
Figure 13: Time dependence of K' with $Ro = 2.75 \times 10^{-2}$, on branch 2. Top: time series; middle: power spectrum of time series (the zero frequency peak has been suppressed); bottom left: delay-space trajectory for the time series.

4.4   The second branch

The numerical results show that there is an additional branch of solutions (which will be referred to as branch two) over at least the range $2.74 \times 10^{-2} \leq Ro \leq 2.85 \times 10^{-2}$, as can be seen in Figure 3. Figure 13 shows a kinetic energy time series for a flow on branch two with $Ro = 2.75 \times 10^{-2}$ (the same value as in Figure 12). The time series is periodic, and now the fundamental frequency is $A/3$. This is not simply a case of B being locked on to $A/3$, since the trajectory does not lie on the torus of branch one.

   A numerical run which has converged to a final state on branch two can be used as an initial condition for a run at a different value of Ro, allowing this branch to be traced out over a range of Ro. Following this procedure it was found that the branch could not be extended for $Ro < 2.74 \times 10^{-2}$ (where it actually seems to be a torus). Further numerical experiments are required in order to understand the disappearance of this branch at lower values of Ro. As Ro is increased the attractor for this branch seems to remain qualitatively similar to that seen at $Ro = 2.75 \times 10^{-2}$, until at $Ro = 2.83 \times 10^{-2}$ it appears that a period-doubling bifurcation has occurred and the basic period becomes $A/6$ (see Figure 14). The behavior of this attractor at
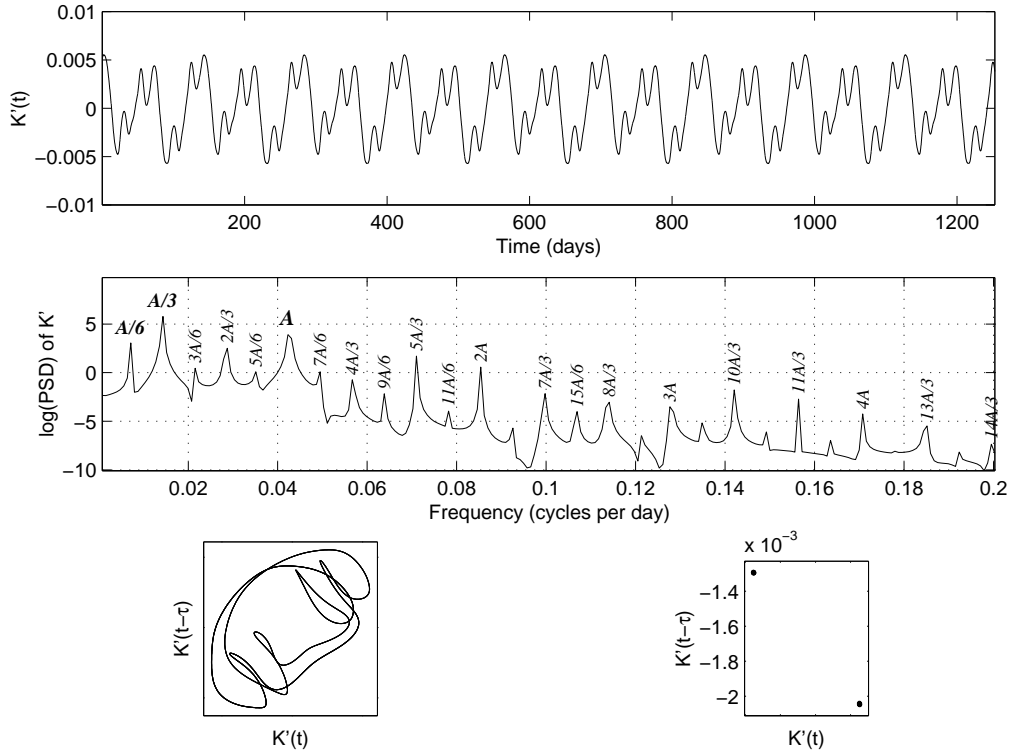
Figure 14: Time dependence of K' with $Ro = 2.83 \times 10^{-2}$, on branch 2. Top: time series; middle: power spectrum of time series (the zero frequency peak has been suppressed); bottom left: delay-space trajectory for the time series; bottom right: Poincaré section of the delay-space trajectory.

larger Ro has not been sufficiently investigated for conclusions to be drawn about the ultimate fate of this branch.

4.5 The path to chaos

The attractor corresponding to the first branch appears to go through several changes for Ro between about 2.75×10^{-2} and 2.90×10^{-2}. At $Ro = 2.79 \times 10^{-2}$ it was found that integrations started from initial conditions on branch one at lower Ro result in a trajectory which quickly leaves the branch one set and converges to the same branch two attractor which is obtained if initial conditions on branch two are used (see Figure 15).

It is tempting to conclude from Figure 15 that the attractor for branch one has become unstable for this Rossby number, leaving the branch two attractor as the only possible final state. However this explanation is less convincing in the light of the results shown in Figure 16 of a run at $Ro = 2.80 \times 10^{-2}$ started from an initial condition on branch one. Integrations started from branch two show convincingly that the second branch is an attracting limit cycle
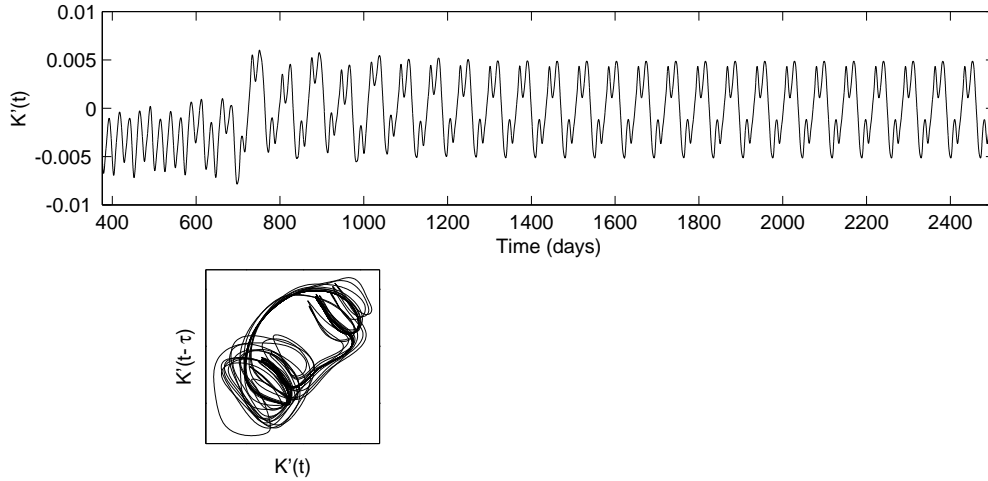
Figure 15: Time dependence of K' with $Ro = 2.79 \times 10^{-2}$ for an integration started from branch 1 initial conditions, but which results in a final state on branch 2. Top: time series; bottom : delay-space trajectory for the time series.

at this Rossby number, yet the trajectory shown in Figure 16 seems unable to converge to the second branch attractor. The trajectory remains mostly in the vicinity of the torus seen at lower Ro, but displays intermittent excursions on trajectories close to the branch two attractor. It is possible that the system would eventually settle on the branch two attractor, but there is no indication that this will happen from the time series of 5000 days shown Figure 16.

At $Ro = 2.85 \times 10^{-2}$, a run initialized on branch one appears to switch erratically between the two types of behavior (see Figure 17). The second branch was actually discovered by taking the ψ and ζ fields at a time when the trajectory was following type two behavior and using this as an initial condition for a run at lower Rossby number. The alternation between these two types of behavior is very intriguing and further numerical experiments at intermediate values of Ro are needed to understand it fully. It is possible that the original attractors have become joined by a heteroclinic orbit involving an unstable periodic orbit. In order to follow up this possibility it would be necessary to solve for the unstable periodic orbit which remains after the second Hopf bifurcation, and trace its location in phase space as Ro increases.

At larger Ro the trajectory appears to be less closely bound to either of the original attractors, perhaps indicating that they have both become more strongly unstable. At $Ro = 3.0 \times 10^{-2}$ the trajectory bears no obvious resemblance to either original attractor (see Figure 18). The power spectrum has become broad-band (a hallmark of chaos) but the peak at A can still be discerned. Runs at $Ro = 4.0 \times 10^{-2}$ and $Ro = 5.2 \times 10^{-2}$ were also chaotic, with broad-band power spectra.
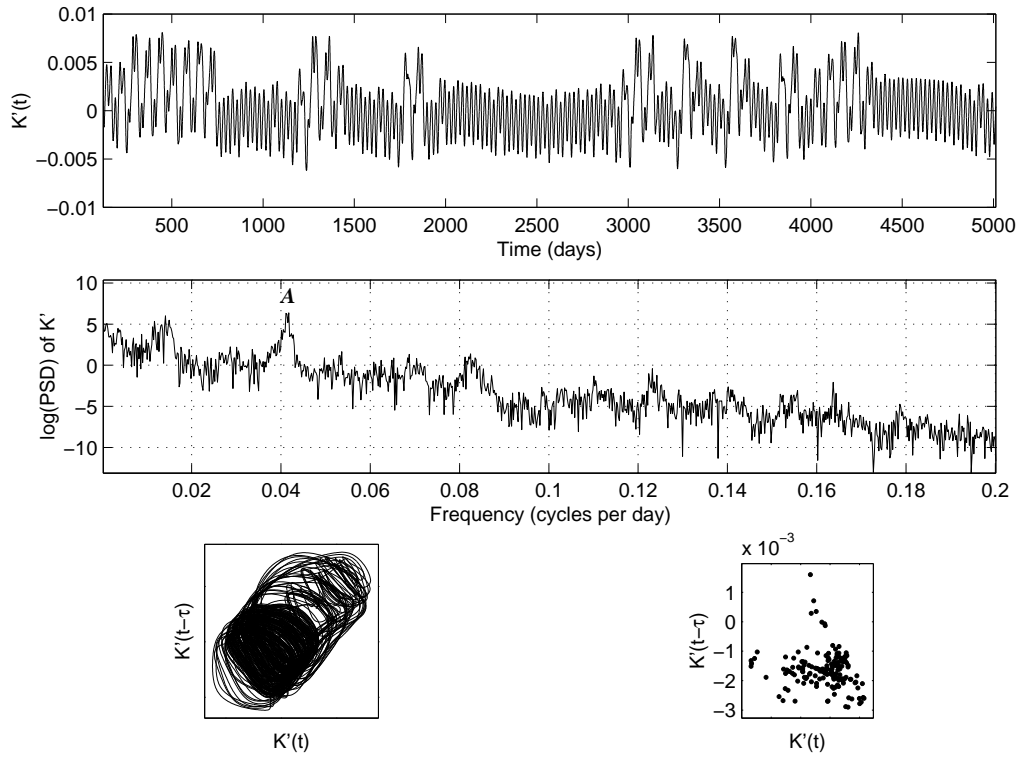
Figure 16: Time dependence of K' with $Ro = 2.80 \times 10^{-2}$ for an integration started from branch 1 initial conditions. Top: time series; middle: power spectrum of time series (the zero frequency peak has been suppressed); bottom left: delay-space trajectory for the time series; bottom right: Poincaré section of the delay-space trajectory.
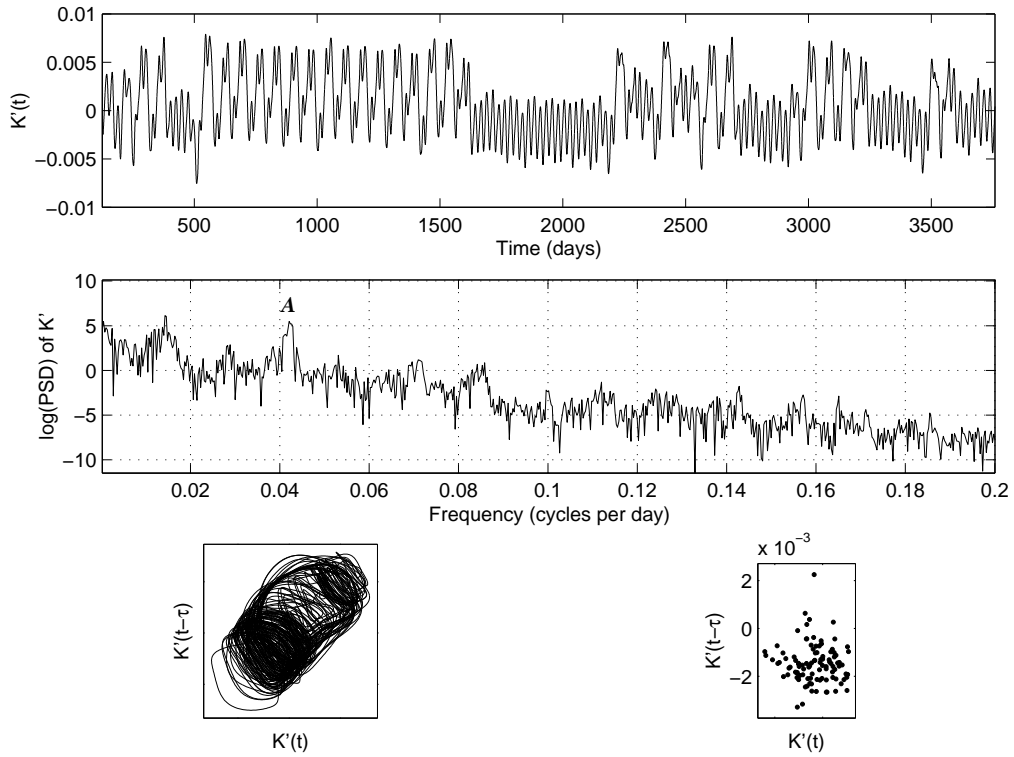
Figure 17: Time dependence of K' with $Ro = 2.85 \times 10^{-2}$ for an integration started from branch 1 initial conditions. Top: time series; middle: power spectrum of time series (the zero frequency peak has been suppressed); bottom left: delay-space trajectory for the time series; bottom right: Poincaré section of the delay-space trajectory.

Figure 18: Time dependence of K' with $Ro = 3.0 \times 10^{-2}$ for an integration started from branch 1 initial conditions. Top: time series; middle: power spectrum of time series (the zero frequency peak has been suppressed); bottom left: delay-space trajectory for the time series; bottom right: Poincaré section of the delay-space trajectory.
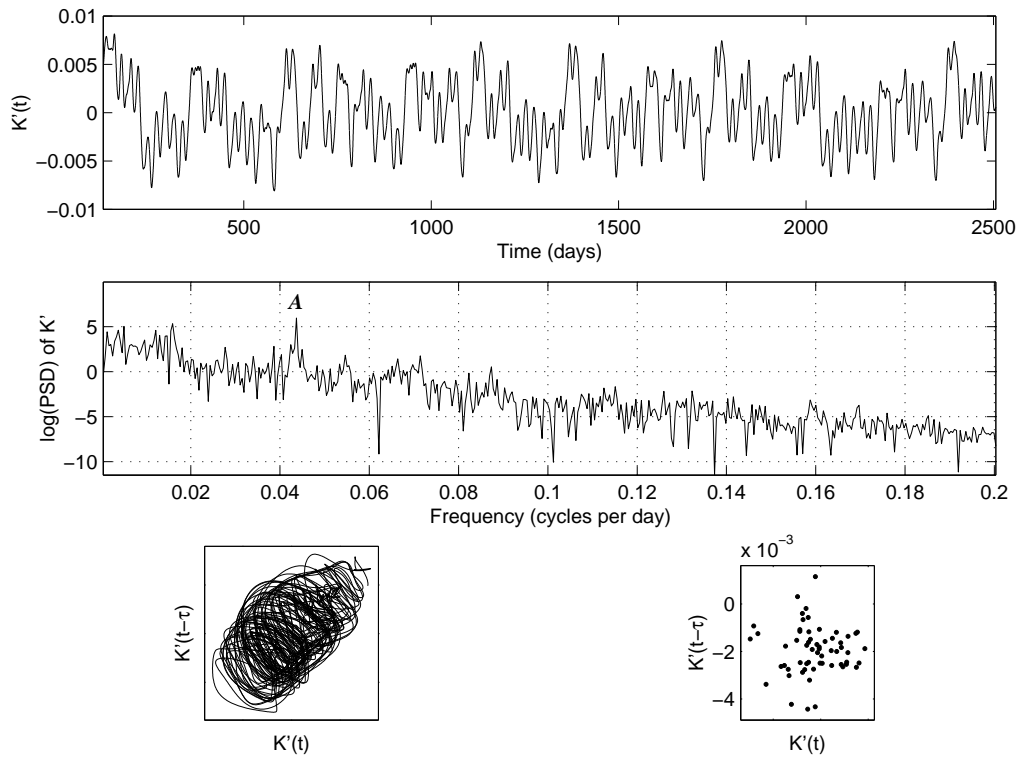
5   Conclusions

The numerical results reported here show that the sliced cone model can display a great richness of complicated behavior including multiple attracting states and a transition to chaos. These results are of particular interest because the model can be realized in the laboratory, allowing the study of low-dimensional chaos in a real physical system. In particular these results show that the transitions from a fixed point to a limit cycle and then to a torus take place via Hopf bifurcations. At larger Rossby number the behavior of the system becomes more complex. A second solution branch appears which coexists with the original branch at moderate Ro. As Ro increases the time series appear to become intermittent when started from the original branch, switching erratically between oscillations characteristic of each branch. These transitions become more frequent at larger Ro, until at $Ro \approx 2.9 \times 10^{-2}$ the delay space trajectory bears little resemblance to either branch and the behavior seems to be chaotic for all larger values of Ro.

6   Future work

There remain several interesting avenues for future study of this system. These include an elucidation of the mechanism by which the flow becomes chaotic (which could involve interaction with unstable periodic orbits or unstable fixed points), and the extent of the second branch as a function of Rossby number. Much longer time series are needed to better understand the chaotic dynamics above $Ro \approx 2.85 \times 10^{-2}$. A sufficiently long time series may show that the Poincaré map is a fractal set, and allow the fractal dimension of the chaotic attractor to be calculated. Longer time series could also clarify whether the erratic behavior seen for $2.80 \times 10^{-2} \leq Ro \leq 2.85 \times 10^{-2}$ is truly chaotic or a chaotic transient.

The behavior of the system as a function of E is yet to be studied using these techniques, and it would be interesting to discover more about the suppression of the anticyclonic instability as E is increased.

The insights provided by this numerical approach to the sliced cone also open up new lines of enquiry using the laboratory apparatus. It would be interesting to look in the laboratory for some of the features of the numerical results, such as the second branch and the intricate dependence of the flow behavior on Ro in the transition from a toroidal attractor to chaos. If time series could be obtained from the flow in the laboratory, the same delay-space techniques could be applied to laboratory data, allowing a detailed comparison with the numerical results. However this would be technically demanding, since the variations in velocity and pressure are very difficult to detect.

7   Acknowledgments

References

[Beardsley, 1975a] Beardsley, R. C. (1975a). A numerical investigation of a laboratory analogy of the wind-driven ocean circulation. In *NAS Symposium on Numerical Models of Ocean Circulation, Durham, New Hampshire, 1972*, page 311, Washington DC. National Academy of Sciences.

[Beardsley, 1975b] Beardsley, R. C. (1975b). The 'sliced-cylinder' laboratory model of the wind-driven ocean circulation, part 2: Oscillatory forcing and Rossby wave resonance. *J. Fluid. Mech.*, 69(1):41–64.

[Becker and Salmon, 1997] Becker, J. M. and Salmon, R. (1997). Eddy formation on a continental slope. *J. Mar. Res.*, 55:181–200.

[Bennetts and Hocking, 1973] Bennetts, D. A. and Hocking, L. M. (1973). On nonlinear Ekman and Stewartson layers in a rotating fluid. *Proc. R. Soc. Lond. A.*, 333:469–489.

[Berloff and Meacham, 1997] Berloff, P. S. and Meacham, S. P. (1997). The dynamics of an equivalent-barotropic model of the wind-driven circulation. *J. Mar. Res.*, 55(3):407–451.

[Griffiths and Veronis, 1997] Griffiths, R. W. and Veronis, G. (1997). A laboratory study of the effects of a sloping side boundary on wind-driven circulation in a homogeneous ocean model. *J. Mar. Res.*, 55:1103–1126.

[Griffiths and Veronis, 1998] Griffiths, R. W. and Veronis, G. (1998). Linear theory of the effect of a sloping boundary on circulation in a homogeneous laboratory model. *J. Mar. Res.*, 56:75–86.

[Israeli, 1970] Israeli, M. (1970). A fast implicit numerical method for time dependent viscous flows. *Studies Appl. Math.*, 49(4):327–349.

[Jiang et al., 1995] Jiang, S., Jin, F.-F., and Ghil, M. (1995). Multiple equilibria, periodic, and aperiodic solutions in a wind-driven, double-gyre, shallow-water model. *J. Phys. Oceanogr.*, 25:764–786.

[Kiss and Griffiths, 1998] Kiss, A. E. and Griffiths, R. W. (1998). Flow dynamics in the 'sliced cone' model of wind-driven ocean circulation. In Melbourne, W. H., editor, *13th Australasian fluid mechanics conference, Melbourne, Australia, 1998*, Victoria 3168, Australia. Monash University.

[Meacham and Berloff, 1997] Meacham, S. P. and Berloff, P. S. (1997). Barotropic, wind-driven circulation in a small basin. *J. Mar. Res.*, 55:523–563.

[Page, 1981] Page, M. A. (1981). *Rotating fluids at low Rossby number*. Phd thesis, University College, London.

[Page, 1982] Page, M. A. (1982). A numerical study of detached shear layers in a rotating sliced cylinder. *Geophys. Astrophys. Fluid Dyn.*, 22:51–69.

[Pearson, 1965] Pearson, C. E. (1965). A computational method for viscous flow problems. *J. Fluid Mech.*, 21(4):611–622.

[Pedlosky, 1987] Pedlosky, J. (1987). *Geophysical fluid dynamics*. Springer, New York, 2 edition.

[Pedlosky and Greenspan, 1967] Pedlosky, J. and Greenspan, H. P. (1967). A simple laboratory model for the oceanic circulation. *J. Fluid Mech.*, 27(2):291–304.

[Salmon, 1992] Salmon, R. (1992). A two-layer Gulf Stream over a continental slope. *J. Mar. Res.*, 50:341–365.

[Takens, 1981] Takens, F. (1981). *Dynamical systems and turbulence, Warwick 1980*, volume 898 of *Lecture notes in mathematics*. Springer-Verlag, Berlin.